Inorganic Chemistry

Article

pubs.acs.org/IC

# Preparation, Formation, and Structure of $[(SnSe)_{1.04}]_m(MoSe_2)_n$ Intergrowth Compounds ($0 < m$ and $n < 32$) from Designed Precursors

Matt Beekman,[†,‡] Sabrina Disch,[†,§] Noel Gunning,[†] and David C. Johnson*,[†]

[†]Department of Chemistry, University of Oregon, Eugene, Oregon 97403, United States

[‡]Department of Natural Sciences, Oregon Institute of Technology, Klamath Falls, Oregon 97601, United States

[§]Department of Chemistry, Universität zu Köln, D-50939 Köln, Germany

S *Supporting Information*

**ABSTRACT:** A detailed synthetic approach, using the method of modulated elemental reactants, is described for the preparation of $MX-TX_2$ (M = metal, X = chalcogen, and T = transition metal) solid-state intergrowths with *m* and *n* values significantly larger than previously reported. As a specific example, we demonstrate the ability to synthesize more than 500 distinct intergrowth compounds in a single ternary system, Sn−Mo−Se. A simple method for determination of the chemical composition of the constituent layers in the precursor and product is described for cases in which both structural components contain one or more common elements. X-ray reflectivity, laboratory and synchrotron X-ray diffraction, scanning transmission electron microscopy, and high-resolution transmission electron microscopy imaging, and electron microprobe analysis provide conclusive evidence of the formation of layered intergrowths with well-defined structure and composition. The ability to access a large range of monochalcogenide thicknesses allows a size-dependent structural transition in the SnSe component to be controlled and tracked and indicates that intergrowth materials such as those described here comprise novel material systems in which size-dependent phenomena can be precisely controlled.

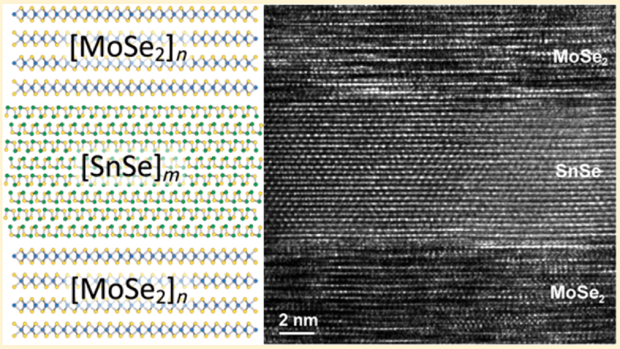

## I. INTRODUCTION

Prof. John Corbett, a leading figure in the solid-state chemistry community for more than 50 years, succinctly highlighted the inherent challenges in the synthesis of solid-state compounds and the limitations of conventional high-temperature reactions in preparative inorganic chemistry (paraphrased):[1]

> *Solid-state reactions and the successful synthesis of single-phase, homogeneous [solid-state] products are often very much at the mercy of intrinsically slow (but still highly variable) rates of diffusion and mass transfer within and between solid particles. The use of high enough temperatures during synthesis improves these rates, but a consequence of this is that much solid-state chemistry at lower temperatures is lost.*

These challenges are intrinsically different from those associated with the synthesis of discrete molecules.[2] Taking advantage of higher diffusion rates in liquid- or vapor-phase systems can increase mass-transfer rates but can complicate the system by increasing the number of interacting constituents. Indeed, Prof. Corbett was known for his "healthy skepticism regarding the real composition of a phase, particularly with respect to the presence of the more pervasive C, N, O and H", which has resulted in many misidentified compounds.[1] Corbett also highlighted the lack of mechanistic information applicable to complicated reaction mixtures, including information on how to control the nucleation of products. While the choice of starting materials can influence thermodynamics and kinetics, the consequence of using elevated temperatures is that most products represent only the thermodynamically most stable phases.[3] As noted by Brewer, there must be many compounds that are stable at low temperatures that cannot be prepared via ordinary means because the rates of formation are too slow at the temperatures at which the compounds would be stable.[4]

A number of low-temperature synthesis routes have been developed that overcome some of the limitations of high-temperature approaches. These include utilizing intimately mixed precursors prepared through solution routes or the oxidation of mixed-metal compounds, which reduce the diffusion path lengths for cations to near atomic dimensions.[5] However, such approaches often still require long diffusion lengths for the anions and/or superfluous atoms that are not incorporated into the final product. Novet and Johnson[6] and subsequent work by Jansen et al.[7] have shown that metastable

**Special Issue:** To Honor the Memory of Prof. John D. Corbett

**Received:** October 4, 2014
**Published:** December 2, 2014

compounds can be nucleated from homogeneous amorphous precursors designed to have the same composition as the final product, eliminating the need for the long-range diffusion of unwanted atoms. Topotactic reactions also provide an elegant example, particularly when used in a sequential fashion as done by Wiley et al.,[8,9] allowing complex metastable structures to be accessed while preserving the features of the host structure. While powerful in specific systems, these approaches still do not provide the systematic body of knowledge required to prepare families of metastable compounds of a large variety of structures and compositions.

During the past several years, we have been developing an alternative synthetic procedure based on modulated elemental reactants (MER).[10,11] In this approach, compositionally modulated thin-film precursors are prepared by sequentially depositing elemental layers, maintaining the correct ratio of elements in each layer of the precursor film to form the desired product. By controlling layer thicknesses and the ratio of the elements in the repeating unit, we have shown that new metastable binary and ternary compounds can be prepared by avoiding other crystalline intermediate phases.[12−14] More recently, we have shown that many new intergrowth compounds can be prepared by employing initial precursors of increased complexity that contain two or more regions with compositional modulations on a subnanometer length scale.[15−17] Each region can lower its free energy without long-range diffusion by locally crystallizing a binary, ternary, or higher-order compound with the desired composition, leading to the intergrowths of two or more structures, provided a stable interface exists between the structures. Here we provide a detailed report on the preparation, formation, and structure of intergrowths based on two semiconducting "parent" binary compounds, SnSe and $MoSe_2$, that are receiving significant contemporary interest for potential electronic and energy conversion applications.[18−20] For intergrowths containing a common element in each region, for example, Se in the $[(SnSe)_{1+\delta}]_m(MoSe_2)_n$ intergrowths reported here, characterization and control of the "reaction mixture" in each region, as well as determination of the chemical composition, are more challenging than the formation of a single homogeneous compound. We describe a systematic analytical approach developed to quantitatively extract the ratios of the elements within each region in cases where both constituents contain a common element, enabling the preparation of $MX-TX_2$ semiconductor intergrowths with $m$ and $n$ values much larger than previously reported.[15−17,21,22]

## II. EXPERIMENTAL DETAILS

**Precursor Preparation and Synthesis.** Thin-film precursors were prepared by the method of MER.[6,10−17,22] The elements Sn, Mo, and Se were sequentially deposited on ⟨001⟩ Si substrates in a custom high-vacuum ($10^{-7}$ Torr) physical vapor deposition system.[23] Sn (99.99%, Alfa Aesar) and Mo (99.8%, Alfa Aesar) were deposited by electron-beam evaporation, whereas Se (99.99%, Alpha Aesar) was deposited using an effusion cell. Deposition rates were monitored (but not quantified, vide infra) by quartz crystal microbalances. The total deposited film thicknesses were typically in the range 50−100 nm, depending on the composition and repeat structure. Precursor annealing was performed on a custom Cu hot plate inside a $N_2$-filled glovebox ($O_2$ and $H_2O$ content < 1 ppm).

**Sample Characterization.** Laboratory X-ray reflectivity (XRR) and X-ray diffraction (XRD) was collected in specular geometry using a Bruker D8 Discover diffractometer equipped with a Göbel mirror and parallel beam optics. The film composition was determined by electron probe microanalysis (EPMA) using a Cameca SX-50 microanalyzer. Element standards and specialized analysis techniques developed for thin-film samples were used to quantify the chemical composition of the films.[24]

In-plane synchrotron XRD data were collected at the 33-BM-C beamline at the Advanced Photon Source (APS) at Argonne National Laboratory using the X-ray energy $E$ = 13.1 keV (wavelength $\lambda$ = 0.99188 Å) and a Vortex point detector. In situ synchrotron XRD data were collected at the 6-ID-D beamline of the APS using synchrotron radiation of energy $E$ = 86.76 keV ($\lambda$ = 0.1429 Å). In order to minimize loss of Se and sample oxidation during heating, the sample was mounted under an Ar atmosphere inside a small-volume custom-made airtight sample container with kapton windows. The amorphous precursor of targeted composition was oriented with the substrate normal perpendicular to the incident X-ray beam, and the sample was dynamically rocked through a small angle during data collection to sample a larger region of reciprocal space. The sample was heated to temperatures of 300, 400, 500, 525, 550, 600, and 650 K; the temperature was measured by a thermocouple placed near the sample holder. At each temperature step, the diffraction pattern was recorded on an amorphous Si area detector with a 10 min exposure time and corrected for the dark detector intensity.

Cross-sectional specimens for high-resolution transmission electron microscopy (HRTEM) and scanning transmission electron microscopy (STEM) investigations were prepared by focused-ion-beam milling using an FEI Helios Nanolab D600. The in situ lift-out was accomplished using an Omniprobe 200 microscope. All specimens were cut out and thinned down to 300 nm at 30 kV. The subsequent thinning process was done at 5 kV, followed by cleaning of the specimens at 2 kV, with a final cleaning at 1 kV. HRTEM was carried out at 300 kV using an FEI imaging lens $C_s$ aberration-corrected Titan 80-300 in both transmission (0.78 Å resolution) and scanning transmission (1.34 Å resolution) modes.

## III. RESULTS AND DISCUSSION

**Precursor Design and Formation of $[(SnSe)_{1+\delta}]_m[MoSe_2]_n$.** The guiding concept underlying the preparation of the $[(SnSe)_{1+\delta}]_m[MoSe_2]_n$ intergrowths is illustrated schematically in Figure 1. A modulated precursor film is prepared that has a spatial profile of composition that is very close to the profile of the final intergrowth product. The relatively high free energy of the precursor can be rapidly lowered by formation of the metastable SnSe−$MoSe_2$ intergrowth in which the constituent atoms adopt more favorable local bonding environments. As a result of the composition

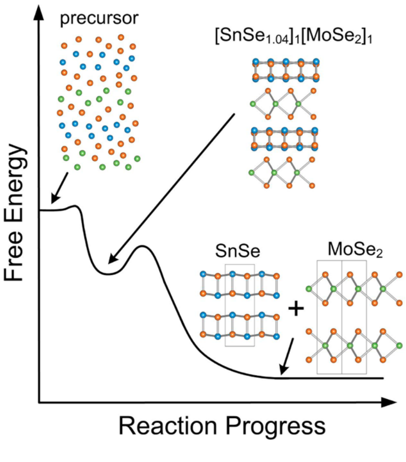

**Figure 1.** Schematic representation of the presumed free-energy diagram relating the modulated precursor, metastable intergrowth, and thermodynamic products. (The structural sequence in the precursor and product is repeated along the axial direction in the film.)

profile in the precursor, the atoms need not travel far to achieve this lower-energy configuration, and the reaction can complete at relatively low temperatures compared to those required for conventional solid-state reactions. The SnSe−$MoSe_2$ intergrowth is an intermediate to the formation of the thermodynamic products, in this case a two-phase mixture of SnSe and $MoSe_2$. If the activation energy for decomposition (and long-range atomic diffusion) of the intergrowth is not surmounted, the metastable intergrowth will be kinetically trapped.

Implicit in Figure 1, the precursor film must have the correct compositional profile for the target intergrowth to form. In the case of homogeneous nucleation of a single compound from a uniform amorphous MER precursor, only the correct ratio of the elements (overall composition) is required, provided the layer thicknesses are sufficiently small to form an amorphous intermediate.[12−14] The preparation of intergrowths, however, requires the absolute amount of each element deposited in each region to be equal to the amount required to locally form the constituent layers, in this case SnSe and $MoSe_2$. Thus, in order to successfully scale the number of layers *m* and *n*, it is not only necessary that the overall composition be correct, the ratio and absolute amount of each element must locally be correct in the regions intended to nucleate the constituents.

Because the Sn−Se and Mo−Se layers in the $[(\mathrm{SnSe})_{1+\delta}]_m[\mathrm{MoSe}_2]_n$ precursor and product both contain Se, measurement of the overall composition by EPMA, which provides the total Se content, does not immediately yield the fraction deposited in each precursor layer or the fraction incorporated in the constituent layers of the product. Nevertheless, through collection of EPMA compositions and low-angle XRD data from an appropriate series of precursors, the ratios of the elements in each deposited bilayer and corresponding thicknesses can be determined in a straightforward manner. Although each element is deposited separately, the binary constituents are deposited in paired "bilayers", and the overall composition in the repeating unit of the precursor can be expressed as $[(\mathrm{Sn|Se}_x)_y]_p|[\mathrm{Mo|Se}_z]_q$, where *p* is the number of Sn−Se bilayers deposited in the repeating unit, *q* is the number Mo−Se bilayers deposited, *x* is the atomic ratio Se:Sn in each Sn−Se bilayer, *y* is atomic ratio Sn:Mo for $p = q = 1$, and *z* is the atomic ratio Se:Mo in each Mo−Se bilayer. We use the symbol "|" to describe the composition of the precursor to distinguish this representation from the common nomenclature for chemical compounds. Multiplying through all coefficients, the overall composition of the precursor can be equivalently written as $\mathrm{Sn}_{yp}|\mathrm{Mo}_q|\mathrm{Se}_{xyp+zq}$.

We designed precursors such that $m = p$ and $n = q$, although, in principle, other precursor structures may be possible. EPMA compositions are collected from a set of precursors in which *p* is increased while *q* is held fixed and vice versa. As shown in Figure 2, appropriately plotting the overall atomic ratios yields linear graphs from which the ratios of Se:Sn and Se:Mo in each of the bilayers can be extracted by linear fits to the data. For example, for fixed $p = 1$ and increasing *q*, a plot of *q* times the total Se:Mo ratio for each precursor yields a straight line whose slope and intercept can be interpreted as *z* and the product *xy*, respectively:

$$q(\mathrm{Se{:}\ Mo}) = q\left(\frac{xyp + zq}{q}\right) = zq + xy$$

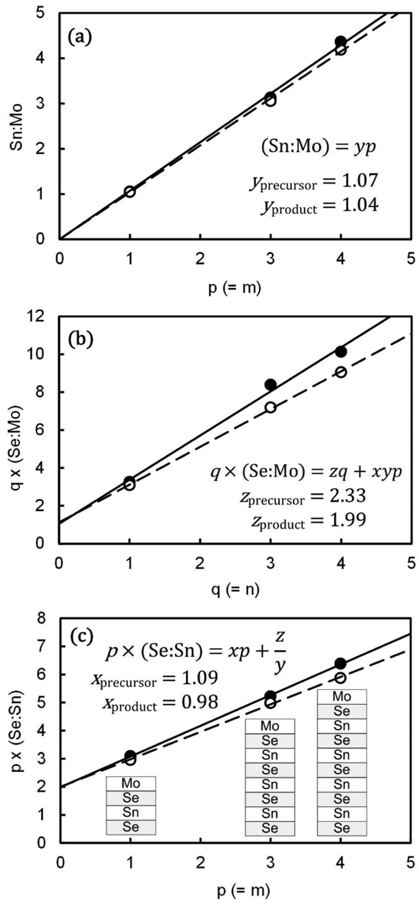

**Figure 2.** Illustration of the method for determining the composition ratios of elements deposited in each bilayer. Various atomic ratios in modulated precursors (●) and annealed products (○), as determined by EPMA, for (a and c) a series of samples with $q = 1$ and increasing *p* and (b) a series of samples with $p = 1$ and increasing *q*. For each case, the equations describe how the contribution of each deposited layer to the total composition can be extracted from these data. The deposition sequence for the repeat unit in the precursors in parts a and c is also shown.

The values of *x* and *y* can similarly be determined for both the precursor and product, as illustrated in Figure 2 for an optimized series of precursors. As shown in Figure 2, the annealed products have $x = 0.98$, $y = 1.04$, and $z = 1.99$, which are in good agreement with the expected compositions (vide infra) within experimental uncertainty. We note that the observation of the expected linear dependence of composition on *p* and *q* shown in Figure 2 indicates that the composition of the bilayers remains consistent (within uncertainty) as the periodic modulation is repeated during deposition. On the basis of the information obtained on the composition of the precursors, the exposure times for each element during deposition can be scaled iteratively until the desired composition is achieved. Upon annealing under an inert atmosphere, it is apparent that some Se is lost because of the high vapor pressure of this constituent; thus inclusion of 10 to 15 at % excess Se in the precursor bilayers is beneficial is included in the precursor (Figure 2).

Although long-range order is essentially lacking in the precursor, the average periodic electron density that results from the modulated composition in the direction perpendicular to the substrate produces limited multilayer Bragg diffraction at

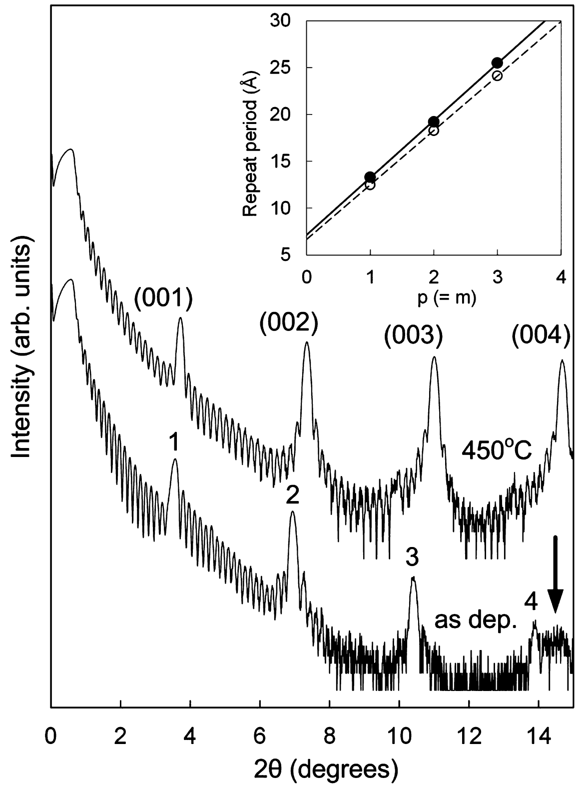

**Figure 3.** XXR data collected from a modulated precursor designed to form the $[(\mathrm{SnSe})_{1.04}]_3[\mathrm{MoSe}_2]_1$ compound (bottom). Also shown (top) are data for the same precursor annealed at 450 °C for 30 min. The arrow indicates the weak (004) reflection (bottom) from the product, which has begun to form under ambient conditions. Inset: Plot of the repeat period for a series of precursors (●) and annealed products (○) for which $q = 1$ and $p$ is increased.

low angles, which can be used to characterize layer thicknesses in the precursor. This is illustrated in Figure 3, which shows an XXR pattern collected from an as-deposited precursor designed to form the $[(\mathrm{SnSe})_{1.04}]_3[\mathrm{MoSe}_2]_1$ compound. The regular oscillations in the intensity at low angles (Kiessig fringes) originate from the interference of X-rays coherently scattered from the top and bottom interfaces of the film, from which the total film thickness can be determined. From the positions of the multilayer Bragg diffraction peaks, the repeat period of the modulation in the precursor can be determined. With the number of deposited Mo−Se layers $q$ held fixed and the number of Sn−Se layers $p$ increased, a plot of the repeat period versus $p$ exhibits a linear relationship (inset to Figure 3), from the slope of which the effective thickness of the Sn−Se bilayer can be determined. This information is complementary to the composition information obtained from analysis of the data shown in Figure 2. The effective thicknesses of the bilayers are also iteratively scaled (holding their ratios fixed) until the optimized precursors are obtained. As shown in Figure 3 (inset), the optimal precursor period is slightly larger than the intergrowth period of the product.

To form the $[(\mathrm{SnSe})_{1+\delta}]_m[\mathrm{MoSe}_2]_n$ intergrowth from a modulated elemental precursor, sufficient energy must be input to overcome activation energies for local atomic rearrangement yet insufficient for long-range diffusion and formation of the thermodynamically most stable products. The optimal temperature and time for product formation are a priori not known and are determined empirically by qualitative and quantitative analysis of XRD data. As an example, Figure 4 shows laboratory XRD data for a precursor designed to form the $[(\mathrm{SnSe})_{1.04}]_4[\mathrm{MoSe}_2]_1$ compound, sectioned into eight equal pieces of equal size and annealed for 30 min at the temperatures indicated. The appearance of two "004" reflections from the precursor film in Figure 3, one corresponding to the modulated precursor and the other to the product, indicates the presence of small regions in which the product has begun to form (weakly ordered) under ambient conditions during deposition. 00*l* reflections corresponding to the product are also visible in the high-angle XRD data from the as-deposited precursor in Figure 4. As the temperature is increased, the 00*l* reflections corresponding to the product grow significantly in intensity up to 723 K, above which a reduction in the intensity is accompanied by the appearance of diffraction peaks from the binary phases, suggesting decomposition of the metastable intergrowth. The reduction in the repeat period upon annealing (Figure 3 inset) reflects a reduction in volume per atom, to be expected as more favorable atomic packing arrangements are achieved in the formation of the intergrowth, as well as some loss of Se (Figure 2b,c). Rocking curves for selected 00*l* reflections as a function of the annealing time at 723 K exhibited an increase in the intensity and a narrowing of the width that showed no significant change after 30 min, suggesting that this is the optimal annealing time for this system.

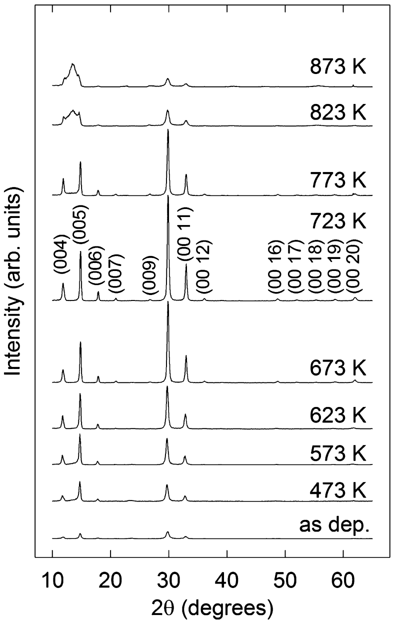

**Figure 4.** Laboratory specular XRD data tracking the formation, then decomposition, of $[(\mathrm{SnSe})_{1.04}]_4[\mathrm{MoSe}_2]_1$.

To gain further insight into the nature of intergrowth formation in the case of large $m$, an in situ annealing study was also carried out using a precursor designed to yield $[(\mathrm{SnSe})_{1.04}]_{12}[\mathrm{MoSe}_2]_{12}$. The temperature-dependent diffraction data obtained in the vicinity of the (00*l*) superlattice reflections as well as the (11±1) reflections of the binary constituent SnSe are presented in Figure 5. As observed in previous studies of intergrowth materials prepared by MER[15,16,22] and discussed further below, (*hkl*) reflections corresponding to the overall intergrowth structure are not observed for $h, k \neq 0$. Rather, because of turbostratic disorder between the SnSe and $\mathrm{MoSe}_2$ layers, independent (*hkl*)

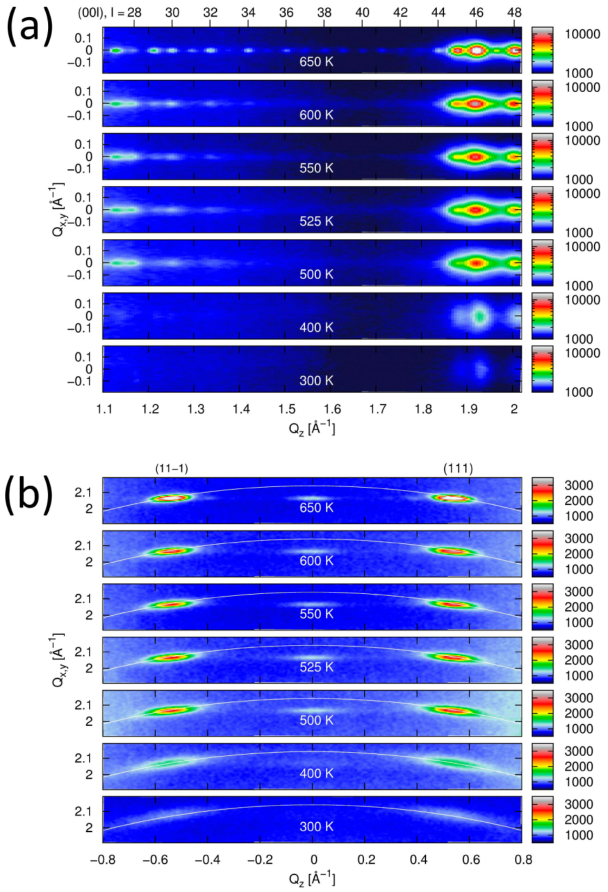

**Figure 5.** Temperature-dependent synchrotron XRD collected during annealing of a precursor designed to form $[(SnSe)_{1.04}]_{12}[MoSe_2]_{12}$: (a) (00$l$) series of superlattice reflections; (b) (111) and (11−1) reflections of the SnSe binary constituent. The thin white curve in part b has been added as a guide to the eye representing the position of SnSe Debye−Scherrer rings that would be expected for a completely randomly oriented powder.

diffraction from the SnSe and $MoSe_2$ constituents is observed. Both reflection series in Figure 5 exhibit reflection profiles that sharpen and increase in intensity with increasing temperature, with significant change appearing in the 400−500 K range. The (00$l$) superlattice reflections presented in Figure 5a exhibit a further noticeable increase in the reflection intensity and sharpness at 600−650 K.

In addition to the (00$l$) reflection width and intensity, the distribution of the intensity for the SnSe constituent reflections represented in Figure 5b provides insight into the formation. Weak SnSe reflections already present in the as-deposited precursor have intensity distributed along the Debye−Scherrer rings characteristic of a slightly textured powder, evidence that a distribution of SnSe nanocrystallite orientations is present upon nucleation. However, we do not observe a completely random orientation, which suggests that interfacial nucleation occurs prior to complete interdiffusion and homogeneous nucleation in the Sn−Se region. With increasing temperature, the reflection intensity distribution evolves into a profile that is broadened along the $Q_z$ direction and narrow along the $Q_{x,y}$ direction, corresponding to the short correlation length due to the limited layer thickness and the somewhat larger correlation length in plane, respectively. Whereas some change in the intensity distribution is already occurring between 400 and 500 K, the most prominent change is observed between 600 and 650 K, the highest temperatures of our measurement. This evolution in the intensity distribution can be attributed to the consumption of SnSe domains that are initially nucleated in slightly off-axis orientations by energetically more favorable highly oriented SnSe domains as the temperature is increased and the intergrowth becomes more structurally organized.

The observation of a "two-step" formation process by a stepwise increase in the reflection intensity of the (00$l$) series along with an increase in the texture (decrease in angular fwhm) is more clearly revealed by quantitative fitting of the temperature-dependent reflection profiles (Figure S1 in the Supporting Information, SI). The first stepwise increase in the (00$l$) intensity at 400−500 K (Figure S2 in the SI) can be attributed to the initial relaxation and interdiffusion of the precursor, eliminating free volume and defects that are relatively mobile. This is manifested in the significant increase in reflection intensities and the sharpening of the reflections, corresponding to an increase in the atomic correlation length. Further growth of the intergrowth domains occurs at higher temperatures with the second step in formation, initiating near 600−650 K. This may be induced by the higher species mobility at elevated temperatures, leading to increased diffusion rates and consistent with the optimal annealing temperature of 723 K observed in the ex situ annealing study in Figure 4.

**Structure of SnSe−$MoSe_2$ Intergrowths.** The formation of well-defined layered intergrowths of SnSe and $MoSe_2$ is confirmed by laboratory and synchrotron XRD and HRTEM and STEM imaging. As an example, Figure 6 shows specular XRD patterns collected from a selection of compounds with $m = n$ ranging from 1 to 12 (component thicknesses corresponding to $^1/_2$ and 6 unit cells of the bulk structures of SnSe and $MoSe_2$, respectively), plotted on a log scale to allow even the weakest reflections to be revealed. All observed

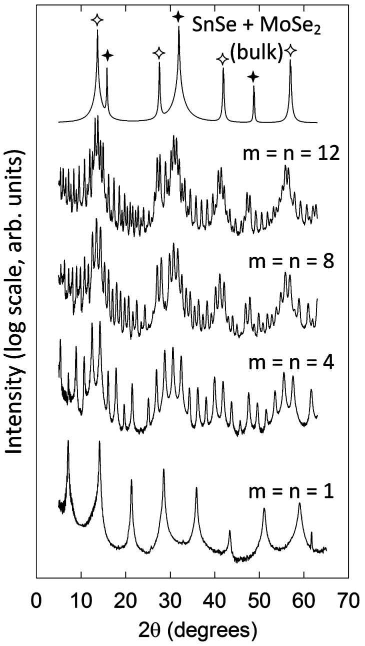

**Figure 6.** Specular XRD patterns collected from $[(SnSe)_{1+\delta}]_m[MoSe_2]_n$ compounds with $m = n = 1$, 4, 8, and 12. Also shown (top) is a simulated diffraction pattern (00$l$ reflections only) for a bulk two-phase mixture of SnSe (◆) and $MoSe_2$ (◇), corresponding to $m = n \to \infty$.

diffraction maxima in each pattern can be indexed very well (see Figure S3 in the SI) as 00*l* reflections using a single *c*-axis parameter corresponding to the overall period of the intergrowth along the axial direction. Also shown in Figure 6 for qualitative comparison are simulated XRD patterns (00*l* reflections only) based on the room temperature bulk SnSe[25] and $MoSe_2$[26] crystal structures (two-phase mixture). Although in the case of an intergrowth the position and intensity (structure factor) of each 00*l* diffraction peak are determined by the overall intergrowth structure, i.e., no individual 00*l* reflection can be solely attributed to scattering from the separate SnSe or $MoSe_2$ components, it is clear that the diffracted intensity for larger *m* and *n* is highest near the positions of the individual maxima corresponding to the bulk structures. Moreover, the relative intensities appear to approach the features in the bulk diffraction patterns in the limit $m, n \to \infty$. Because the specular diffraction profile is obtained via Fourier transform of the periodic electron density along the axial (*c*) direction, this suggests that the weighting of the Fourier components needed to describe the composite intergrowth structure is comparable to that required for the sum of the independent constituents. While detailed modeling of these complex structures using specular diffraction is difficult given the limited number of diffraction observations and large number of structural parameters required, this qualitative observation suggests that basic features of the bulk structures are retained upon formation of the intergrowth.

As expected, plotting the *c*-axis parameter (intergrowth period, *c*) versus $m = n$ reveals a systematic increase with $m = n$ (Figure 7). Deviation of each *c*-axis lattice parameter from *n* times the period for the $m = n = 1$ compound is expected because increasing *m* and *n* by 1 adds a SnSe bilayer and a $MoSe_2$ trilayer to the unit cell but does not add additional SnSe−$MoSe_2$ interfaces, which remain constant at two per period for all compositions. If the addition of SnSe and $MoSe_2$ components has a constant thickness contribution, the deviation of each measured lattice parameter $c_{n,n}$ from *n* times the *c* parameter for the $m = n = 1$ compound, $nc_{1,1} - c_{n,n}$, is expected to be equal to the difference $(n - 1)(c_{2,2} - 2c_{1,1})$, i.e., $n - 1$ times the deviation of the 2,2 compound from twice the *c* parameter for $m = n = 1$. Plotting $nc_{1,1} - c_{n,n}$ versus $(n - 1)(c_{2,2} - 2c_{1,1})$ shows that the deviation can indeed be primarily attributed to the difference in the number and type of interfaces as $m = n$ is increased above 1. The slightly larger deviation for $m = n = 8$ and 12, which corresponds to a slightly smaller than expected *c* parameter for these compounds, can be attributed to a size-induced structural transition that occurs in the SnSe component,[27] which is discussed in more detail below.

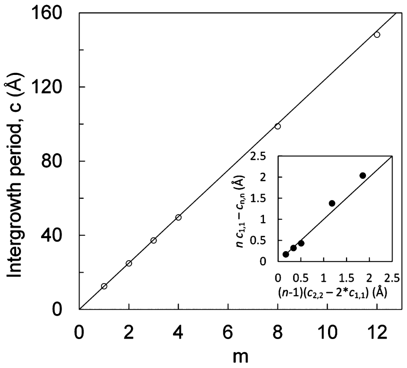

**Figure 7.** Intergrowth period versus $m = n$. The straight line is the linear trend if the period were simply $nc_{1,1}$. Inset: Actual deviation of the observed period for each compound from $nc_{1,1}$, i.e., $nc_{1,1} - c_{n,n}$, plotted against the expected deviation $(n - 1)(c_{2,2} - 2c_{1,1})$ based on the difference between the 1,1 and 2,2 compounds that results from the presence of different interfaces. All compositions with $m = n > 1$ have periods smaller than the expected trend, with a deviation that becomes larger with increasing *n*.

Using the synthetic approach discussed above, we have successfully prepared $[(SnSe)_{1.04}]_m[MoSe_2]_n$ with *n* as large as 16 and *m* as large as 31, although we expect that still larger *m* and *n* are likely possible. Table 1 lists a selection of compounds that we have obtained along with their *c*-lattice parameters. In contrast to some examples in the structurally related conventional misfit layered compounds[28] and also in MER-prepared PbSe−$MoSe_2$ intergrowths,[22] we have not observed SnSe-based compounds with half-integer values of *m*, corresponding to a half-layer (monolayer) increment of SnSe. This difference can be understood by considering the bulk crystal structures of PbSe and SnSe. PbSe crystallizes in the cubic NaCl (rock salt) structure, whereas SnSe crystallizes in the layered orthorhombic GeS (distorted rock salt) structure. In the case of SnSe, the energetic favorability for forming a layered structure with relatively strong intralayer and weaker interlayer interactions likely results in too high of an energy penalty for the formation of half-integer *m* (*m* = 1.5, 2.5, 3.5, etc.) corresponding to intergrowth structures that cannot accommodate the layered structure of the SnSe component. Although we have not directly synthesized every possible $[(SnSe)_{1.04}]_m[MoSe_2]_n$ variant, interpolating the possible combinations of *m* and *n* suggested by Table 1 indicates that more than 500 distinct compounds in this single ternary system can be synthetically accessed by the approach we have described above.

**Table 1. Compositions (Indicated by *m* and *n*) and Measured *c* Parameters for 23 Different $[(SnSe)_{1.04}]_m[MoSe_2]_n$ Compositions**[a]

| *m* | *n* | *c* (Å) | *m* | *n* | *c* (Å) | *m* | *n* | *c* (Å) |
|---|---|---|---|---|---|---|---|---|
| 1 | 1 | 12.50 | 12 | 12 | 148.26 | 16 | 2 | 105.53 |
| | | 12.52 | 16 | 16 | 191.47 | 21 | 2 | 134.31 |
| | | 12.52 | 1 | 2 | 19.04 | 27 | 2 | 168.72 |
| 2 | 2 | 24.88 | 1 | 3 | 25.63 | 10 | 4 | 84.14 |
| | | 24.88 | 2 | 1 | 18.28 | 12 | 4 | 95.68 |
| 3 | 3 | 37.25 | 3 | 1 | 24.12 | 16 | 4 | 118.63 |
| 4 | 4 | 49.66 | 12 | 1 | 76.04 | 21 | 4 | 147.43 |
| | | 49.66 | 4 | 2 | 36.46 | 26 | 4 | 176.23 |
| 8 | 8 | 98.81 | 9 | 2 | 65.38 | 31 | 4 | 204.84 |

[a] Multiple samples of the same nominal composition are included for three compositions (*m* = *n* = 1, *m* = *n* = 2, and *m* = *n* = 4). The uncertainty in the lattice parameters is approximately 0.01 Å.

As shown in Figure 8, HREM and STEM imaging confirmed the layering of SnSe and $MoSe_2$ in well-defined intergrowths. The distinct SnSe and $MoSe_2$ layers can be clearly discerned, while the overall intergrowth periods are in good agreement with those determined from XRD. The HRTEM data reveal significant turbostratic disorder within each repeating unit of the $MoSe_2$ component, which is consistent with the structure of group 6 diselenides prepared by MER.[22,29] In contrast, the SnSe component appears to form coherent "blocks" that are limited in thickness by the top and bottom interfaces with $MoSe_2$ (Figure 8d). The intergrowths of SnSe and $MoSe_2$ can

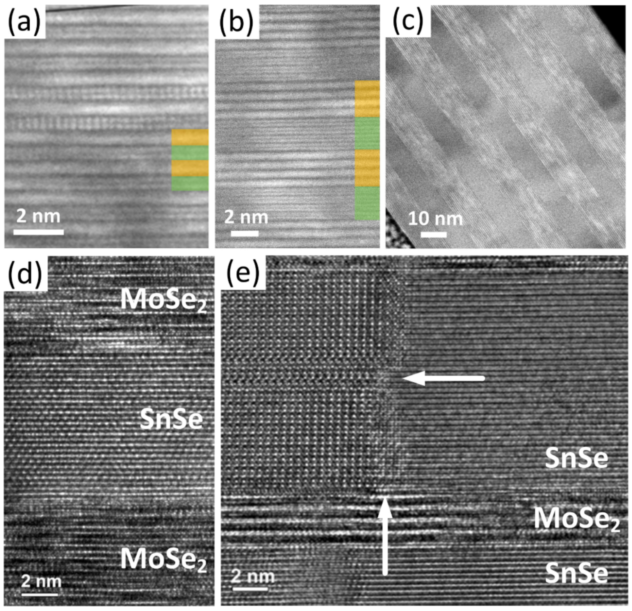

**Figure 8.** HAADF STEM images collected from compounds with (a) $m = n = 1$, (b) $m = n = 4$, and (c) $m = n = 16$. In parts a and b, the SnSe and MoSe$_2$ layers are highlighted in orange and green, respectively. Image c shows that the uniform-layered structure persists through the entire thickness of the film. (d) HRTEM image from the same sample shown in part c. (e) HRTEM data from a sample with $m = 21$ and $n = 4$. The vertical arrow indicates a SnSe interlayer grain boundary. The horizontal arrow indicates SnSe stacking faults.

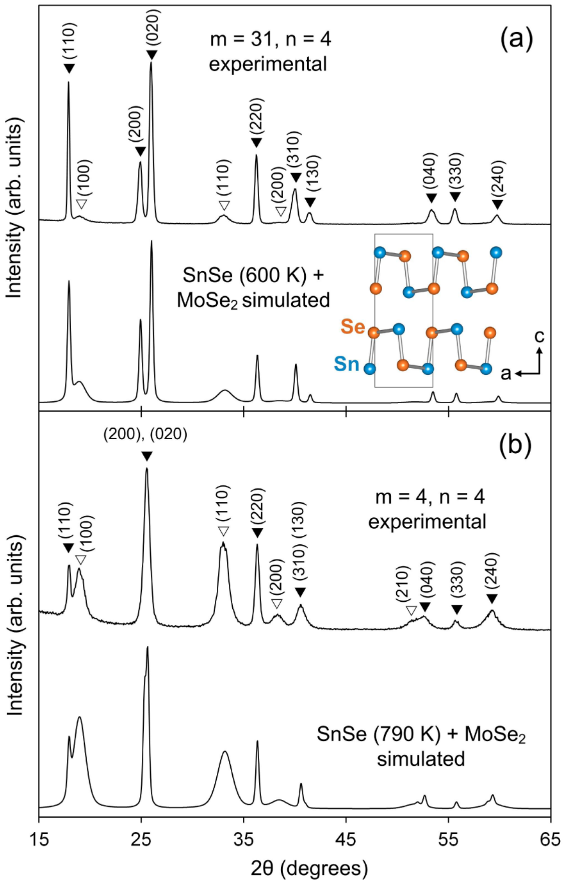

**Figure 9.** Experimental synchrotron XRD patterns collected from $[(\mathrm{SnSe})_{1+\delta}]_m[\mathrm{MoSe}_2]_n$ with (a) $m = 31$ and $n = 4$ and (b) $m = n = 4$. SnSe (▼) and MoSe$_2$ (▽) ($hk0$) reflections are indicated. Also shown are simulated ($hk0$) diffraction patterns for two-phase mixtures of bulk 2H−MoSe$_2$[26] and $\alpha$-SnSe.[25] The structure for bulk $\alpha$-SnSe corresponds to neutron refinement at the indicated temperature. Inset: Crystal structure of bulk $\alpha$-SnSe at 600 K used for the simulations.

therefore be described as precisely stacked nanocrystalline layers, which have little to no long-range order with respect to each other in any direction other than the axial direction. This interpretation is supported by synchrotron XRD collected using an area detector,[27] which shows only *hkl* reflections that can be indexed to the individual components, and the lack of any *hkl* reflections attributed to the overall intergrowth structure, in contrast to ordered incommensurate intergrowth crystals. The processes of nucleation and growth during precursor annealing determine the resulting rotational disorder in the MoSe$_2$ component,[30] which is apparently related to the negligible energy differences between different stacking polytypes. Although bulk SnSe also has a layered crystal structure with strong intralayer covalent bonding and weaker interlayer interactions,[25] the interlayer interactions are significantly stronger than those in MoSe$_2$, and no turbostratic disorder is observed. While our TEM observations indicate that SnSe typically forms coherent blocks with thickness $m$ and no intralayer turbostratic disorder, we have on occasion also observed stacking faults such those indicated in the HRTEM image in Figure 8. An in-plane "grain boundary" between two SnSe nanodomains is also visible in this image.

In contrast to specular XRD data, which contain only 00$l$ reflections from the overall intergrowth (Figure 6), synchrotron diffraction data collected using an in-plane geometry show only $hk0$ reflections originating from the individual SnSe and MoSe$_2$ components (Figure 9). This observation, and the lack of any *hkl* reflections that can be attributed to the overall intergrowth structure,[27] is consistent with highly oriented SnSe and MoSe$_2$ domains that do not possess long-range interlayer coherence and therefore diffract as independent nanocrystalline domains. All reflections in the in-plane diffraction patterns can be indexed to either a hexagonal unit cell corresponding to MoSe$_2$ or an orthorhombic unit cell corresponding to SnSe. The lattice parameter for MoSe$_2$ is independent of $n$ within the uncertainty and has the constant value of $a = 3.31$ Å. This value is slightly larger than the basal-plane lattice parameter for bulk MoSe$_2$[26] and in good agreement with the value reported for PbSe−MoSe$_2$,[22] suggesting that the second constituent does not have a significant effect. In contrast, as the thickness of the SnSe layer is reduced, a size-induced structural transition occurs in which the basal-plane lattice parameters simultaneously approach a common value (Figure 10).[27] The behavior of the basal-plane lattice parameters in $[\mathrm{SnSe}]_m$ is similar to that of the continuous $\alpha$-SnSe → $\beta$-SnSe second-order structural phase transition occurring in bulk SnSe crystals as the temperature is increased, which has been studied in detail by temperature-dependent single-crystal neutron diffraction.[25]

At room temperature, bulk $\alpha$-SnSe crystallizes in the orthorhombic GeS structure (space group *Pbnm*). This structure is characterized as a double-layer distorted rock salt structure with a single crystallographic site each for Sn and Se with positional parameters ($x$, $y$, $^1/_4$). As the temperature is increased and the basal-plane and axial lattice parameters evolve, the positional parameters also continuously change: the basal-plane positional parameter $y$ increases only slightly for Se and Sn, the $x$ positional parameter for Se increases slightly, and

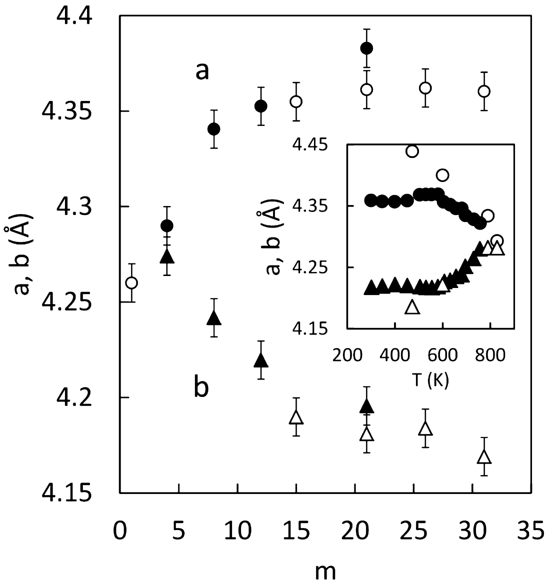

**Figure 10.** Basal-plane lattice parameters versus *m* for the SnSe component: *a* parameter (circles) and *b* parameter (triangles) as determined from synchrotron area diffraction (closed symbols) and in-plane diffraction (open symbols). Inset: Temperature dependence of *a* and *b* for the $m = n = 12$ compound (closed symbols) and bulk SnSe crystals (open symbols).

the *x* parameter for Sn decreases dramatically from $x = 0.1035$ to 0. At 829 K, the structure of $\beta$-SnSe is best described as the higher-symmetry TlI structure (space group *Cmcm*).[25]

Given that the axial size of the SnSe nanocrystalline domains is constrained to be equal to the thickness of the layer, *m*, the similar behavior of the basal-plane lattice parameters with increasing temperature for bulk SnSe and with decreasing size for $[\mathrm{SnSe}]_m$ suggests a size-induced structural phase transition akin to similar transitions in other chalcogenides[31,32] and oxides.[33,34] This interpretation is supported by simulated[35] XRD patterns (*hk*0 reflections only) comprising a two-phase mixture of SnSe and $\mathrm{MoSe_2}$, shown in Figure 9 for comparison to the experimental in-plane synchrotron diffraction patterns for $(m, n) = (4, 4)$, and (31, 4). The simulated and experimental diffraction patterns show relatively good qualitative agreement, indicating that the basic features of the structure of $[\mathrm{SnSe}]_m$ correspond to those of the bulk structure at higher temperatures (600 and 790 K). Interestingly, even for *m* as large as 31, the structure of $[\mathrm{SnSe}]_m$ corresponds to a high-temperature structure (the bulk lattice parameters are not yet achieved). This can be contrasted with more subtle size-dependent structural distortions that have been observed in analogous PbSe-based intergrowths, distortions that are no longer detectable for $m > 6$.[22] In spite of the evolution of the lattice parameters for SnSe, the misfit parameter, which characterizes the ratio of the in-plane atomic packing density of the cations, remains constant within uncertainty at $\delta = 0.04$ for all *m*.

To further characterize the structure of SnSe, we collected temperature-dependent synchrotron XRD data from the $m = n = 12$ compound, from which the temperature dependence of the basal-plane lattice parameters was determined (Figure 10, inset). Also shown is the temperature dependence of *a* and *b* for bulk $\alpha$-SnSe.[25] The structural transformation in $[\mathrm{SnSe}]_{12}$ shows behavior qualitatively similar to that of bulk SnSe, in which *a* and *b* approach a common value at high temperature. Interestingly, *a* and *b* show only a slight change up to nearly 600 K, above which the basal-plane lattice parameters then rapidly approach a common value. Above 600 K, the similarity to the bulk *a* and *b* lattice parameters indicates that $[\mathrm{SnSe}]_{12}$ is more “bulklike” at higher temperatures than at lower temperatures. Instead of *a* and *b* reaching a common value at a significantly lower temperature than the bulk, extrapolation suggests that they reach their common value at nearly the same temperature, which differs from the behavior of other size-induced structural phase transitions.[34] First-principles calculations suggest that the size-induced structural transition with the layer thickness in $[\mathrm{SnSe}]_m$ can be attributed to the enthalpic contribution to the surface free energy of the competing phases,[27] as evidenced by a predicted structural transition with *m* at 0 K. Presented with the data of Figure 10, we speculate that the vibrational entropy at high temperatures may compete with and overcome the influence of the surface free energy, resulting in a lessened influence of the size on the structure.

Although the SnSe basal-plane parameters become indistinguishable for $m < 4$, the presence of the (110) SnSe reflection for all *m* implies that the structure does not complete the transformation to the $\beta$-SnSe structure for any *m* because this reflection is kinematically forbidden for the $\beta$-SnSe structure. The structure of SnSe at room temperature for all $m > 1$ can therefore be described by the $\alpha$-GeS structure in which the average crystallographic position of the Sn and Se atoms is size-dependent. Although the experimental and simulated (*hk*0) diffraction patterns, in general, show relatively good qualitative agreement in the reflection positions and relative intensities for SnSe, we note that there are significant discrepancies in the two patterns for $\mathrm{MoSe_2}$. In particular, the relative intensities of the (100) and (110) reflections are reversed, indicating that the structure of $\mathrm{MoSe_2}$, while hexagonal, may not be well described by the 2H−$\mathrm{MoSe_2}$ polytype. Moreover, our attempts thus far to refine the in-plane structure of SnSe and $\mathrm{MoSe_2}$ by the Rietveld method have not yielded satisfactory fits, indicating significant deviations of the average structure from the bulk and the limitations of a bulklike model in describing the structures of SnSe and $\mathrm{MoSe_2}$ in these materials.

## IV. CONCLUSIONS

The preparation of Sn−Mo−Se precursors with composition modulations similar to those of the desired final products provides an avenue for preparing a large family of compounds $[(\mathrm{SnSe})_{1+\delta}]_m[\mathrm{MoSe_2}]_n$ with targeted values of *m* and *n*. An approach to determine the composition of the constituent regions of the precursors enables the preparation of compounds with values of *m* and *n* larger than 30. These compounds can be thought of as intergrowths of SnSe and $\mathrm{MoSe_2}$, where the thickness of the layers is precisely controlled. The structure of the SnSe layer depends on the SnSe thickness but differs in some respects from other size-induced phase transitions. We believe this synthesis approach might provide attractive avenues for the preparation of two-dimensional heterostructures.

## ■ ASSOCIATED CONTENT

### Ⓢ Supporting Information

Experimental synchrotron diffraction data and simulated reflection profiles for synchrotron XRD and corresponding reflection profile parameters and lattice parameter determination from linear least-squares fitting. This material is available free of charge via the Internet at http://pubs.acs.org.

## AUTHOR INFORMATION

### Corresponding Author

*E-mail: davej@uoregon.edu.

### Notes

The authors declare no competing financial interest.

## ACKNOWLEDGMENTS

The authors acknowledge support from the National Science Foundation under Grant DMR-1266217. D.C.J. acknowledges support from the National Science Foundation through CCI Grant CHE-1102637. Grant MRI 0923577 provided funding for the dual-beam FIB used to make TEM cross sections. Use of the APS, an Office of Science User Facility operated for the U.S. Department of Energy (DOE), Office of Science, by Argonne National Laboratory, was supported by the U.S. DOE under Contract DEAC02-06CH11357. The authors thank Dr. Sergei Rouvimov and Prof. Dr. Wolfgang Neumann for their assistance with HRTEM and STEM data collection, Jenia Karapatrova and Dr. Paul Zschack (33-BM-C, APS) and Doug Robinson (6-ID-D, APS) for their assistance in the collection of synchrotron XRD data, and C. Heideman and D. Moore for many useful discussions.

## DEDICATION

Dedicated to the memory of Professor John Corbett, a long-time mentor and friend to many in the solid-state chemistry community.

## REFERENCES

(1) Corbett, J. D. In *Solid State Chemistry Techniques*; Cheetham, A. K., Day, P., Eds.; Oxford Science Publications: Oxford, U.K., 1990.

(2) DiSalvo, F. J. *Science* **1990**, *247*, 649–655.

(3) Stein, A.; Keller, S. W.; Mallouk, T. E. *Science* **1993**, *259*, 1558–1564.

(4) Brewer, L. *J. Chem. Educ.* **1958**, *35*, 153–156.

(5) West, A. R. *Solid State Chemistry and Its Applications*, 2nd ed.; John Wiley and Sons: New York, 2014.

(6) Novet, T.; Johnson, D. C. *J. Am. Chem. Soc.* **1991**, *113*, 3398–3403.

(7) Liebold-Ribeiro, Y.; Fischer, D.; Jansen, M. *Angew. Chem., Int. Ed.* **2008**, *47*, 4428–4431.

(8) Viciu, M. L.; Caruntu, G.; Koenig, J.; Zhou, W. L.; Kodenkandath, T. A.; Wiley, J. B. *Inorg. Chem.* **2002**, *41*, 3385–3388.

(9) Viciu, M. L.; Koenig, J.; Spinu, L.; Zhou, W. L.; Wiley, J. B. *Chem. Mater.* **2003**, *15*, 1480–1485.

(10) Johnson, D. C. *Curr. Opin. Solid State Mater. Sci.* **1998**, *3*, 159–167.

(11) Noh, M.; Johnson, C. D.; Hornbostel, M. D.; Thiel, J.; Johnson, D. C. *Chem. Mater.* **1996**, *8*, 1625–1635.

(12) Fukuto, M.; Hornbostel, M. D.; Johnson, D. C. *J. Am. Chem. Soc.* **1994**, *116*, 9136–9140.

(13) Hornbostel, M. D.; Hyer, E. J.; Thiel, J. P.; Johnson, D. C. *J. Am. Chem. Soc.* **1997**, *119*, 2665–2668.

(14) Anderson, M. D.; Thompson, J. O.; Johnson, D. C. *Chem. Mater.* **2013**, *25*, 3996–4002.

(15) Heideman, C. L.; Nguyen, N.; Hanni, J.; Lin, Q. Y.; Duncombe, S.; Johnson, D. C.; Zschack, P. *J. Solid State Chem.* **2008**, *181*, 1701–1706.

(16) Lin, Q. Y.; Smeller, M.; Heideman, C. L.; Zschack, P.; Koyano, M.; Anderson, M. D.; Kykyneshi, R.; Keszler, D. A.; Anderson, I. M.; Johnson, D. C. *Chem. Mater.* **2010**, *22*, 1002–1009.

(17) Beekman, M.; Heideman, C. L.; Johnson, D. C. *Semicond. Sci. Technol.* **2014**, *29*, 064012–1–064012–14.

(18) Li, L.; Chen, Z.; Hu, Y.; Wang, X.; Zhang, T.; Chen, W.; Wang, Q. *J. Am. Chem. Soc.* **2013**, *135*, 1213–1216.

(19) Huang, C.; Wu, S.; Sanchez, A. M.; Peters, J. J. P.; Beanland, R.; Ross, J. S.; Rivera, P.; Yao, W.; Cobden, D. H.; Xu, X. *Nat. Mater.* **2014**, DOI: 10.1038/NMAT4064.

(20) Zhao, L.-D.; Lo, S.-H.; Zhang, Y.; Sun, H.; Tan, G.; Uher, C.; Wolverton, C.; Dravid, V. P.; Kanatzidis, M. G. *Nature* **2014**, *508*, 373–377.

(21) Beekman, M.; Cogburn, G.; Heideman, C.; Rouvimov, S.; Zschack, P.; Neumann, W.; Johnson, D. C. *J. Electron. Mater. (Proc. Int. Conf. Thermoelectr. 2011)* **2012**, *41*, 1476–1480.

(22) Heideman, C. L.; Tepfer, S.; Lin, Q.; Rostek, R.; Zschack, P.; Anderson, M. D.; Anderson, I. M.; Johnson, D. C. *J. Am. Chem. Soc.* **2013**, *135*, 11055–11062.

(23) Fister, L.; Li, X. M.; McConnell, J.; Novet, T.; Johnson, D. C. *J. Vac. Sci. Technol. A* **1993**, *11*, 3014–3019.

(24) Phung, T. M.; Jensen, J. M.; Johnson, D. C.; Donovan, J. J.; McBurnett, B. G. *X-ray Spectrom.* **2008**, *37*, 608–614.

(25) Chattopadhyay, T.; Pannetier, J.; von Schnerring, H. G. *J. Phys. Chem. Solids* **1986**, *47*, 879–885.

(26) James, P. B.; Lavik, M. T. *Acta Crystallogr.* **1962**, *16*, 1183–1183.

(27) Beekman, M.; Disch, S.; Rouvimov, S.; Kasinathan, D.; Koepernik, K.; Rosner, H.; Zschack, P.; Neumann, W. S.; Johnson, D. C. *Angew. Chem., Int. Ed.* **2013**, *52*, 13211–13214.

(28) Cario, L.; Lafond, A.; Palvadeau, P.; Deudon, C.; Meerschaut, A. *J. Solid State Chem.* **1999**, *147*, 58–67.

(29) Chiritescu, C.; Cahill, D. G.; Nguyen, N.; Johnson, D.; Bodapati, A.; Keblinski, P.; Zschack, V. *Science* **2007**, *315*, 351–353.

(30) Atkins, R.; Moore, D. B.; Johnson, D. C. *Chem. Mater.* **2013**, *25*, 1744–1750.

(31) Tolbert, S. H.; Alivisatos, A. P. *Science* **1994**, *265*, 373–376.

(32) Chen, C.-C.; Herhold, A. B.; Johnson, C. S.; Alivisatos, A. P. *Science* **1997**, *276*, 398–401.

(33) McHale, J. M.; Auroux, A.; Perrotta, A. J.; Navrotsky, A. *Science* **1997**, *277*, 788–791.

(34) Ayyub, P.; Palkar, V. R.; Chattopadhyay, S.; Multani, M. *Phys. Rev. B* **1995**, *51*, 6135–6138.

(35) Kraus, W.; Nolze, G. *J. Appl. Crystallogr.* **1996**, *29*, 301–303.